PHYSICAL REVIEW C VOLUME 23, NUMBER 5 MAY 1981

Dirac optical model analysis of $\vec{p}$-^{40}Ca elastic scattering at 180 MeV and the wine-bottle-bottom shape

L. G. Arnold and B. C. Clark
Department of Physics, The Ohio State University, Columbus, Ohio 43210

R. L. Mercer
Thomas J. Watson Research Center, International Business Machines Corporation, Yorktown Heights, New York 10598

P. Schwandt
Indiana University Cyclotron Facility, Bloomington, Indiana 47405
(Received 13 January 1981)

A Dirac equation optical model calculation with the real part of the optical potential constrained by relativistic model considerations is used to represent 180 MeV $\vec{p}$-^{40}Ca elastic scattering data. The Dirac equation optical potential consists of a mixture of Lorentz scalar and Lorentz vector potentials. Features of an effective Schrödinger equation optical potential constructed from these two potentials are deduced and compared with results from the standard optical model.

[NUCLEAR REACTIONS Relativistic optical model; ^{40}Ca(p,p), T_p=181 MeV, calculated $\sigma(\theta)$ and $A(\theta)$; deduced effective optical potential.]

I. INTRODUCTION

During the past few years an optical model for nucleon-nucleus elastic scattering based on the Dirac equation has been developed as an alternative to the standard Schrödinger equation formulation.[1,2] The essential feature of this model is the treatment of the optical potential as a mixture of Lorentz scalar and Lorentz vector potentials. A model of this type was formulated over 20 years ago by Duerr[3]; however, his work predated the discovery of the heavy mesons, which are now thought to play an important role in the description of nuclei, and was not widely applied. More recent work with relativistic models has been remarkably successful in the treatment of both finite nuclei and nuclear matter.[4-31] In general, these works consider the nucleon-nucleon interaction to be mediated, in the main, by the exchange of scalar and vector bosons. Thus, the simplest relativistic treatment of the many-body problem, using meson exchange ideas as a basis, contains Lorentz scalar and Lorentz vector components as the dominant features of the nuclear single particle potential.

In the work described here, which has as its underlying motivation an eventual relativistic description of the nucleon-nucleus interaction, some features of the Lorentz transformation character of the optical potential are explored. These features are a general consequence of using a relativistic wave equation such as the Klein-Gordon or Dirac equation as opposed to the Schrödinger equation. A relativistic optical model (ROM) (Ref. 32) containing static Lorentz scalar and vector potentials may result in an effective Schrödinger equation optical potential which exhibits a transition region in bombarding energy where the potential changes from attraction at low energies to repulsion at high energies. An effect of this type is not possible for the Schrödinger equation with a static potential. This feature is of particular interest for nucleon-nucleus scattering where the real part of the empirical optical potential is known to change from attraction to repulsion between 150 and 500 MeV. The availability of new data from IUCF and TRIUMF provides the opportunity to begin exploring the empirical transition region in considerable detail. Additionally, this energy range is important for nonrelativistic theoretical optical model formulations in that the Glauber, KMT, or Watson[33-35] methodologies are applicable above 200 MeV while the BHF and g-matrix approaches are appropriate at lower energies.[36-38]

One of the more interesting consequences of the relativistic optical model in the transition energy region is that the real effective optical potential can deviate considerably from a Fermi-distribution-like shape customarily associated with the nuclear density even when the individual Lorentz scalar and vector potentials have Fermi-distribution-like shapes. That an unorthodox shape could be required to fit experimental data in this energy

range was first noted by Elton[39] for p-^{56}Fe and has been confirmed in recent work by Meyer *et al.*[40] for $\vec{p}$-^{12}C. One of the purposes of this paper is to investigate the possible relativistic origin of this behavior. A calculation of the effective Schrödinger equation single particle potential from a Dirac-Hartree model by the Liège group[27-30] shows that it changes from a smooth Fermi-like shape at low energies to a wine-bottle-bottom shape in the transition region. Above the transition region a Fermi-like shape is recovered, but it has a smaller rms radius than the real effective potential at low energies.[2,41,42] In this paper we show that the unorthodox shape is consistent with a relativistic optical model treatment of nucleon-nucleus scattering in the transition region. In particular, we investigate the recent 181 MeV $\vec{p}$-^{40}Ca cross section and analyzing power data from the IUCF, and find that the real part of the effective potential which produces agreement with experiment has an anomalous shape.

In Sec. II we describe the $\vec{p}$-^{40}Ca experiment. The Dirac equation optical model and $\vec{p}$-^{40}Ca analysis are discussed in Sec. III. In Sec. IV we compare the effective Schrödinger equation optical potential deduced from the analysis with phenomenological and theoretical results obtained from the standard Schrödinger equation based optical model.

II. EXPERIMENT

The experimental data for $\vec{p}$-^{40}Ca elastic scattering at 181 MeV bombarding energy presented here were obtained at IUCF as part of a larger program of differential cross section and analyzing power measurements for polarized proton elastic and inelastic scattering from a range of nuclei for proton energies between 80 and 200 MeV.

The present measurements were carried out using the polarized proton beam from the Indiana University cyclotron accelerator system. The beam intensity on target varied from a few to 30 nA, depending on the scattering angle. The beam polarization was typically 67%. It was measured periodically during the experiment by $\vec{p}$-^{4}He elastic scattering between the first and second cyclotron stages where the beam energy was 13.8 MeV and the analyzing power is accurately known. Self-supporting targets of 10 to 35 mg/cm^2 isotopically enriched ^{40}Ca were used. The scattered protons were detected with good energy resolution (< 200 keV) using a magnetic spectrograph which employed a focal-plane detection system consisting of a helical wire chamber for position information and two plastic scintillators for particle identification. The spectrograph horizontal acceptance angle was set to $\Delta\theta = 0.5°$ at forward angles and $\Delta\theta = 1.0°$ at large angles. The angular range covered in the present experiment was $\theta_{lab} = 7.5°$–$63.5°$ in $1.5°$ to $2.0°$ steps. For each angle setting runs of about equal beam charge were taken with the spin vector of the incident protons oriented up and down with respect to the scattering plane. Changing spin state was accomplished by switching radiofrequency transitions in the atomic-beam polarized ion source. Charge integration and automatic beam centering on target was achieved by stopping the transmitted beam in a split carbon beam stop. Analyzing powers and relative differential cross sections were calculated from normalized spin-up, spin-down detector yields in the usual way after correction for dead-time losses. Absolute normalization of the differential cross sections is believed to be in error by less than ± 10%, mainly due to uncertainty in the measured target thickness.

III. RELATIVISTIC OPTICAL MODEL

In this section we discuss the relativistic optical model developed previously for low and intermediate energy nucleon-nucleus scattering[1,2] and apply it in an analysis of the 180 MeV $\vec{p}$-^{40}Ca elastic scattering data. The construction of effective Schrödinger equation central and spin orbit potentials from the Lorentz vector and scalar potentials is included at the end of the section.

The optical potential consists of two parts: one, $U_0(r)$, which transforms like the timelike component of a Lorentz four-vector; the other, $U_s(r)$, is a Lorentz scalar. The Dirac equation with these potentials is ($\hbar = c = 1$)

$$\{\vec{\alpha}\cdot\vec{p} + \beta[m + U_s(r)] + [U_0(r) + V_C(r)]\}\Psi(\vec{r}) = E\Psi(\vec{r}), \tag{1}$$

where $V_C(r)$ is the Coulomb potential for protons determined from the empirical nuclear charge distribution, m the nucleon mass, and E the nucleon total energy in the c.m. frame. Interactions which have any Lorentz character consistent with conservation laws could be used in Eq. (1). The restriction to local vector and scalar potentials is motivated by conservation laws as applied to real, static potentials and by meson exchange considerations which suggest that these potentials represent the most important interactions. The complex potentials are written

$$U_0(r) = V_0 f_0(r) + iW_0 g_0(r), \tag{2}$$

$$U_s(r) = V_s f_s(r) + iW_s g_s(r), \tag{3}$$

with the form factors chosen to be two-parameter Fermi-type functions $[1 + \exp(r - c)/z]^{-1}$. Thus,

taken as a strictly phenomenological model, there are twelve adjustable parameters, the same number as for a phenomenological Schrödinger equation based optical model using Fermi-type functions for the complex central potential and derivatives of Fermi-type functions for the complex spin orbit potential. In the relativistic model all spin dependent effects are implicit in the Dirac equation.

The Lorentz vector and scalar potentials given in Ref. 1 are used as a constraint in the present analysis. Specifically, the form factors associated with these potentials are used to prescribe the Fermi-type function form factors $f_0(r)$ and $f_s(r)$ for the real parts of $U_0(r)$ and $U_s(r)$ in Eqs. (2) and (3) which are then taken to be fixed. This theoretically based fixed geometry prescription reduces the number of adjustable parameters in the analysis from twelve to eight. While it was initially intended as a guide, it has been found to work well enough without modification to obtain good fits to p-^{40}Ca elastic scattering data from 25 MeV to 1 GeV.[42,43] With this in mind, we review the construction of the potentials given in Ref. 1 with emphasis on those factors which influence their geometry.

A. Real parts of U_0 and U_s

The Lorentz vector and scalar potentials given in Ref. 1 are

$$V_0(r) = \mathrm{Re}U_0(r) = \int d\vec{r}' v_0(|\vec{r}-\vec{r}'|)\tilde{\rho}_0(r'), \tag{4}$$

$$V_s(r) = \mathrm{Re}U_s(r) = \int d\vec{r}' v_s(|\vec{r}-\vec{r}'|)\tilde{\rho}_s(r'), \tag{5}$$

where $v_0(r)$ and $v_s(r)$ are regarded as effective interactions for point nucleons interacting via exchange of point mesons, $\tilde{\rho}_0(r)$ and $\tilde{\rho}_s(r)$ are effective densities obtained by folding a structure profile for projectile and target nucleons with point nucleon target matter densities $\rho_0(r)$ and $\rho_s(r)$. Hadronic structure effects, which are essential to a realistic construction, are incorporated through the use of effective densities; these are related to the point nucleon matter densities by[44]

$$\tilde{\rho}_{0,s}(r) = \int\int d\vec{r}' d\vec{r}'' \rho_b(|\vec{r}''-\vec{R}|)\rho_b(|\vec{r}''+\vec{R}|)\rho_{0,s}(r'), \tag{6}$$

where $\rho_b(r)$ is the structure profile and $\vec{R} = (\vec{r}-\vec{r}')/2$. We take $\rho_b(r)$ to be a Gaussian with unit normalization and rms radius $\langle r_b^2\rangle^{1/2} = 0.8$ fm as a measure of hadronic structure or finite size effects. The precise value adopted for $\langle r_b^2\rangle^{1/2}$ is not a critical factor in the present analysis so long as it is a typical 0.7–0.9 fm hadron size.

The effective interactions are written

$$v_0(r) = t_0 f(\mu_0, r), \tag{7}$$

$$v_s(r) = t_s f(\mu_s, r), \tag{8}$$

where the form factor $f(\mu, r)$ is taken to be a Yukawa with unit normalization and mass parameter μ. The effective interaction volume integrals t_0 and t_s are related to Yukawa masses and coupling constants by $t_0 = g_0^2/\mu_0^2$ and $t_s = -g_s^2/\mu_s^2$; the form factor rms radius is related to the mass by $\langle r^2\rangle = 6/\mu^2$. In the mean field approximation, these masses and coupling constants can be identified as the masses and coupling constants of the neutral vector (ω) and scalar (σ) bosons of the one boson exchange model (OBEM) of the two-nucleon interaction. This allows mean field target matter densities and potentials to be calculated using OBEM parameters as primary input. Alternatively, t_0 and t_s can be evaluated in nuclear matter using the binding energy per nucleon and equilibrium baryon density as input with the scalar to baryonic density ratio of nuclear matter $[\rho_s/\rho_0]_{\mathrm{nm}}$ being obtained in the process. These identifications of characteristic parameters are used as a guide in the construction of $v_0(r)$ and $v_s(r)$.

As an alternative to calculating $\rho_0(r)$ in the mean field approximation mentioned above, we use an empirical density determined from electron scattering. This alternative has several advantages: first, it eliminates the mean field approximation density as a source of uncertainty in the optical potential; second, it allows the use of target input which is identical to the input used in microscopic calculations of the optical potential with Schrödinger equation based formalisms; third, it forces independent consideration of $\rho_s(r)$, an empirically undetermined one body density associated with relativistic models, and its relation to $\rho_0(r)$. In this analysis, $\rho_0(r)$ is chosen for convenience to be the Fermi-distribution-like parametrization suggested by Negele[45]; the same density is used in the Liège and Oxford calculations[36-38] of the nonrelativistic optical potential. The parameters for ^{40}Ca are $c = 3.586$ fm and $z = 0.540$ fm, which yields an rms radius of 3.43 fm. The effective density $\tilde{\rho}_0(r)$ obtained from Eq. (8) has an rms radius of 3.61 fm. A Fermi-distribution-like parametrization of $\tilde{\rho}_0(r)$ which preserves the essential features of this folding integral [normalization, rms radius, and $\tilde{\rho}(0)$] is compatible with the use of a Fermi-type function for $\rho_0(r)$.[46] The Fermi-type function for $\tilde{\rho}(r)$ determined in this way has a slightly smaller

range, $c = 3.495$ fm, and is more diffuse, $z = 0.642$ fm, than $\rho_0(r)$. Uncertainties in $V_0(r)$ attributable to $\rho_0(r)$ and $\rho_b(r)$ are empirical in origin and thus common to both relativistic and standard optical model calculations; they are unimportant in a comparison of the models.

The vector potential may be written in the form

$$V_0 = J_0 F(\mu_0, r), \tag{9}$$

where

$$J_0 = t_0 \tag{10}$$

is the volume integral per nucleon and

$$F(\mu_0, r) = \int d\vec{r}' f(\mu_0, |\vec{r} - \vec{r}'|)\tilde{\rho}_0(r') \tag{11}$$

is a form factor normalized to the nucleon number of the target. The rms radius of $F(\mu_0, r)$ is related to the rms radius of $\rho_0(r)$ by

$$\langle R_0^2 \rangle = \langle R_{\rho_0}^2 \rangle + 2\langle r_b^2 \rangle + \langle r_{\mu_0}^2 \rangle. \tag{12}$$

To complete the specification of $F(\mu_0, r)$, we take μ_0 to be the mass of the ω meson as suggested from the mean field approximation. This choice for the finite range of the effective vector interaction ($\mu_0 = 780$ MeV, $\langle r_\mu^2 \rangle^{1/2} = 0.62$ fm) yields $\langle R_0^2 \rangle^{1/2} = 3.66$ fm, a 0.05 fm increase over $\langle R_{\tilde{\rho}_0}^2 \rangle^{1/2}$ The correction in going from $\tilde{\rho}_0(r)$ to $F(\mu_0, r)$ is small enough to be masked by the uncertainties in $\rho_0(r)$ and $\rho_b(r)$. A Fermi-distribution-like parametrization of $F(\mu_0, r)$ analogous to the previous one for $\tilde{\rho}_0(r)$ is used to prescribe the form factor f_0 in Eq. (2). The values $c_0 = 3.474$ fm and $z_0 = 0.668$ fm obtained differ slightly from the values for $\tilde{\rho}_0(r)$ given above. The strength V_0 in Eq. (2) is given by $V_0 = At_0/N_0$, where A is the nucleon number of the target and N_0 is the normalization of $F_0(r)$.

The scalar density $\rho_s(r)$ or the scalar to baryonic density ratio $\rho_s(r)/\rho_0(r)$ is required in the evaluation of $V_s(r)$. This one body property of the target nucleus is subject to the constraint,

$$\rho_s(r)/\rho_0(r) < 1, \tag{13}$$

by definition. It represents an additional element of freedom that is generic to the distinction between relativistic and nonrelativistic models. In contrast to $\rho_0(r)$ which has been systematically probed by electron scattering, $\rho_s(r)$ is empirically undetermined at present; this situation could conceivably change in the future. The bulk effect of any difference between $\rho_s(r)$ and $\rho_0(r)$ is contained in a volume average scalar to baryonic density ratio defined by

$$[\rho_s/\rho_0]_{\text{vol}} = \int d\vec{r}\, \rho_s(r) \Big/ \int d\vec{r}\, \rho_0(r). \tag{14}$$

It is clear from Eq. (13) that

$$\min(\rho_s/\rho_0)_0^\infty < [\rho_s/\rho_0]_{\text{vol}} < 1, \tag{15}$$

where $\min(\rho_s/\rho_0)_a^b$ is the minimum value of $\rho_s(r)/\rho_0(r)$ in the interval $a < r < b$. The upper bound in Eq. (15) may be reduced from unity by noting that

$$[\rho_s/\rho_0]_{\text{vol}} < (1 - \overline{T}/2m)/(1 + \overline{T}/2m), \tag{16}$$

where

$$\overline{T} = \langle \Psi_u | p^2/2m | \Psi_u \rangle / \langle \Psi_u | \Psi_u \rangle \tag{17}$$

is identified as the nonrelativistic average kinetic energy per nucleon of the target ground state. This yields $[\rho_s/\rho_0]_{\text{vol}} \lesssim 0.98$. The lower bound in Eq. (15) can be identified in the idealized limit of a homogenous medium. Here,

$$[\rho_s/\rho_0]_{\text{vol}} = \min(\rho_s/\rho_0)_0^\infty = [\rho_s/\rho_0]_{\text{nm}}, \tag{18}$$

where $[\rho_s/\rho_0]_{\text{nm}}$, the scalar to baryonic density ratio of nuclear matter, is a derived and, thus, highly model dependent quantity in nuclear matter models. Values of $[\rho_s/\rho_0]_{\text{nm}}$ ranging downward from the 0.98 upper bound are possible; however, for those models under serious consideration as a guide to a relativistic description of finite nuclei, the value of $[\rho_s/\rho_0]_{\text{nm}}$ is strongly constrained by the empirical binding energy per nucleon and baryon density of normal nuclear matter. For matter in equilibrium with less than 20 MeV binding energy per nucleon, $[\rho_s/\rho_0]_{\text{nm}} \gtrsim 0.91$ over the range of baryonic density typically found in nuclei. Thus, to the extent that properties of nuclear matter in equilibrium are a reasonable guide to bulk properties of finite nuclei, the relation for finite nuclei corresponding to Eq. (18) for nuclear matter is

$$[\rho_s/\rho_0]_{\text{vol}} \geq \min(\rho_s/\rho_0)_0^\infty \approx \min[\rho_s/\rho_0]_{\text{nm}}, \tag{19}$$

where $\min[\rho_s/\rho_0]_{\text{nm}} \approx 0.91$ for the models considered. It then follows that the bulk effect of the difference between $\rho_s(r)$ and $\rho_0(r)$ is bounded by

$$0.91 \lesssim [\rho_s/\rho_0]_{\text{vol}} \lesssim 0.98. \tag{20}$$

The only limitation on this result, apart from the model dependence of the lower bound, is the customary use of an equilibrium property of nuclear matter to estimate a bulk property of finite nuclei.

The primary geometrical effect associated with the difference between $\rho_s(r)$ and $\rho_0(r)$ is the fractional difference in their mean square radii defined by

$$\epsilon = (\langle R_{\rho_s}^2 \rangle - \langle R_{\rho_0}^2 \rangle)/\langle R_{\rho_0}^2 \rangle$$

$$= \int d\vec{r}\,(r^2/\langle R_{\rho_0}^2 \rangle - 1)\rho_s(r) \Big/ \int d\vec{r}\, \rho_s(r). \tag{21}$$

Contributions from the interior ($r^2 \lesssim \langle R_{\rho_0}^2 \rangle$) and

exterior regions of the integral in the numerator tend to cancel; by treating them separately, ϵ can be bounded as follows:

$$C_l I(\rho_0) < \epsilon < C_u I(\rho_0), \tag{22}$$

where the integral ($x = \langle R_{\rho_0}{}^2 \rangle^{1/2}$)

$$I(\rho_0) = \int_0^x d\vec{r}(1 - r^2/x^2)\rho_0(r) \Big/ \int d\vec{r}\,\rho_0(r) \tag{23}$$

depends only on the baryonic density, while

$$C_u = [\max(\rho_s/\rho_0)_x^\infty - \min(\rho_s/\rho_0)_0^x]/[\rho_s/\rho_0]_{\rm vol} \tag{24}$$

and

$$C_l = [\min(\rho_s/\rho_0)_x^\infty - \max(\rho_s/\rho_0)_0^x]/[\rho_s/\rho_0]_{\rm vol} \tag{25}$$

depend only on $\rho_s(r)/\rho_0(r)$ in the interior or exterior regions as defined by $\langle R_{\rho_0}{}^2 \rangle^{1/2}$. It follows from Eqs. (13) and (18) that

$$C_u < (1 - \min[\rho_s/\rho_0]_{\rm nm})/\min[\rho_s/\rho_0]_{\rm nm} \lesssim 0.1. \tag{26}$$

The same argument applied to C_l yields $C_l = -C_u$. However, $[\rho_s/\rho_0]_{\rm nm}$ increases as the baryonic density decreases over the range of densities encountered in the interior and surface regions of finite nuclei; additionally, a 25% change in baryonic density causes a change in $[\rho_s/\rho_0]_{\rm nm}$ of about 1%. These properties of $[\rho_s/\rho_0]_{\rm nm}$ suggest that the minimum value of $\rho_s(r)/\rho_0(r)$ for $r \geq \langle R_{\rho_0}{}^2 \rangle^{1/2}$ and the maximum value for $r \leq \langle R_{\rho_0}{}^2 \rangle^{1/2}$ will each occur at or near $r = \langle R_{\rho_0}{}^2 \rangle^{1/2}$ and that they will be about equal as a result. From this approximate cancellation it follows that $|C_l|$ can be taken to be zero in comparison with $|C_u|$. Thus the bounds on ϵ are

$$0 \lesssim \epsilon < 0.1\, I(\rho_0), \tag{27}$$

where $I(\rho_0)$ can be evaluated from Eq. (23) for any baryonic density of interest. The upper bound on ϵ for Negele's Fermi-distribution-like parametrization of $\rho_0(r)$ decreases from about 0.03 in ^{16}O to 0.02 in ^{40}Ca and then decreases slightly more to 0.016 in ^{208}Pb. The resulting upper bound on $\langle R_{\rho_s}{}^2 \rangle^{1/2} - \langle R_{\rho_0}{}^2 \rangle^{1/2}$ decreases from 0.04 fm in ^{16}O to 0.035 in ^{40}Ca and then increases to 0.045 fm in ^{208}Pb; thus, it is reasonable to expect that for realistic baryonic densities

$$0 \lesssim \langle R_{\rho_s}{}^2 \rangle - \langle R_{\rho_0}{}^2 \rangle^{1/2} \lesssim 0.05 \text{ fm} \tag{28}$$

throughout the Periodic Table with possible exceptions for very light nuclei such as ^{3}He and ^{4}He which have exceptional baryonic densities.[47]

In the preceding remarks, we have shown that the scalar density does not differ dramatically from the baryonic density for most nuclei. The bulk effect of this difference is at most 10%; the primary geometrical effect is less than about 3% for nuclei heavier than ^{16}O. Both could be ignored by taking $\rho_s(r) \approx \rho_0(r)$ in the absence of compelling circumstances to the contrary. However, the situation in the evaluation of $V_s(r)$ is such that it is necessary to retain the bulk correction. The volume integral per nucleon of $V_s(r)$,

$$J_s = t_s[\rho_s/\rho_0]_{\rm vol}, \tag{29}$$

depends on both t_s and the bulk correction. In this regard, the ratio

$$R_R \equiv J_0/J_s = (t_0/t_s)[\rho_s/\rho_0]_{\rm vol}{}^{-1} \tag{30}$$

may be determined empirically from a Dirac equation optical model analysis to within about 1%[2]; the ratio (t_0/t_s) as obtained from either OBEM parameters for the nucleon-nucleon interaction or relativistic models of nuclear matter is about -0.77 with an uncertainty of 3 or 4%.[2] The small deviation of $[\rho_s/\rho_0]_{\rm vol}$ from unity shown in Eq. (20) is clearly important in this context and requires the bulk correction to be retained. The primary geometrical correction is also relevant. As noted previously,[1] a small difference in the rms radii of $V_s(r)$ and $V_0(r)$, in concert with their nearly equal magnitudes and opposite signs in the nuclear interior, is responsible for a much larger difference between the rms radius of the effective Schrödinger equation central potential $\langle R_{\rm opt}{}^2 \rangle^{1/2}$ and $\langle R_{\tilde{\rho}_0}{}^2 \rangle^{1/2}$. The latter is a well-known empirical effect at low energies which is ascribed in the nonrelativistic optical model[48] to the long range of the form factor for the effective interaction in

$$V_{\rm opt}(r) = \int d\vec{r}'\, v(|\vec{r} - \vec{r}'|)\tilde{\rho}_0(r'). \tag{31}$$

In the relativistic model, using ^{40}Ca as an example, a 0.05 fm difference in $\langle R_s{}^2 \rangle^{1/2}$ and $\langle R_0{}^2 \rangle^{1/2}$ results in a 0.5 fm difference in $\langle R_{\rm opt}{}^2 \rangle^{1/2}$ and $\langle R_{\rho_0}{}^2 \rangle^{1/2}$. Since the rms radii of $V_s(r)$ and $V_0(r)$ are related by

$$\langle R_s{}^2 \rangle - \langle R_0{}^2 \rangle = \epsilon \langle R_{\rho_0}{}^2 \rangle + \langle r_{\mu_s}{}^2 \rangle - \langle r_{\mu_0}{}^2 \rangle, \tag{32}$$

where

$$\langle R_{\rho_s}{}^2 \rangle - \langle R_{\rho_0}{}^2 \rangle = \epsilon \langle R_{\rho_0}{}^2 \rangle \tag{33}$$

is the contribution from the difference between $\rho_s(r)$ and $\rho_0(r)$, the possibility of a 0.035 fm difference in $\langle R_{\rho_s}{}^2 \rangle^{1/2}$ and $\langle R_{\rho_0}{}^2 \rangle^{1/2}$ is notably important. Barring other considerations, it suggests the use of nucleon scattering as a feasible probe of the difference between scalar and baryonic densities analogous to its traditional role as a probe of neutron-proton density differences.[49] Other considerations are currently more important, however, since the rms radii of the effective interactions also contribute to the difference in the rms radii of $V_s(r)$ and $V_0(r)$. Assuming that $\langle r_{\mu_0}{}^2 \rangle$

and $\langle r_{\mu_s}{}^2\rangle$ can be specified from meson mass empirics, the uncertainty in the value of $\langle r_{\mu_0}{}^2\rangle$ is negligibly small; the uncertainty in the value of $\langle r_{\mu_s}{}^2\rangle$ on the other hand is so large that it obscures any distinction which could be made between $\langle R_{\rho_s}{}^2\rangle$ and $\langle R_{\rho_0}{}^2\rangle$. The σ boson, which is used to specify $\langle r_{\mu_s}{}^2\rangle$, simulates a broad mass distribution with centroid in the region 400 to 700 MeV, more or less, that is identified with scalar-isoscalar two pion exchange processes. To the extent that this distribution can be approximated by a discrete mass or a distribution of a few discrete masses, the primary geometrical correction can be included as a nominal shift which lowers the centroid. This correction, while important, need not be retained explicitly in the evaluation of $V_s(r)$. The same result can be obtained by putting all of the uncertainty in the effective scalar interaction f_s. For this purpose the scalar density may be written

$$\rho_s(r)=[\rho_s/\rho_0]_{\rm vol}\,\rho_0(r), \tag{34}$$

with the proviso that geometrical differences between $\rho_s(r)$ and $\rho_0(r)$ be incorporated in the form factor of the effective scalar interaction; it follows that the effective scalar density in Eq. (6) may be written

$$\tilde{\rho}_s(r)=[\rho_s/\rho_0]_{\rm vol}\,\tilde{\rho}_0(r), \tag{35}$$

with the additional proviso that differences in the scalar and baryonic structure profiles [omitted in Eq. (6)] also be incorporated in the form factor of the effective scalar interaction.[50]

The scalar potential may be written

$$V_s(r)=J_s F(\mu_s, r), \tag{36}$$

where the form factor

$$F(\mu_s, r)=[\rho_s/\rho_0]_{\rm vol}{}^{-1}\int d\vec{r}\,' f(\mu_s, |\vec{r}-\vec{r}\,'|)\tilde{\rho}_s(r') \tag{37}$$

is normalized to the nucleon number of the target; this may be written

$$F(\mu_s, r)=\int d\vec{r}\,' f(\mu_s, |\vec{r}-\vec{r}\,'|)\tilde{\rho}_0(r') \tag{38}$$

by making use of Eq. (35) with all geometrical differences between $\tilde{\rho}_s(r)$ and $\tilde{\rho}_0(r)$ incorporated in μ_s. We take $\mu_s=550$ MeV to complete the specification of $F(\mu_s, r)$. This choice[51] yields $\langle R_s{}^2\rangle^{1/2}=3.71$ fm, which is 0.1 fm larger than $\langle R_{\rho_0}{}^2\rangle^{1/2}$ and 0.05 fm larger than $\langle R_0{}^2\rangle^{1/2}$. Apart from the 0.05 fm difference between $\langle R_s{}^2\rangle^{1/2}$ and $\langle R_0{}^2\rangle^{1/2}$ which is essential, the correction in going from $\tilde{\rho}_0(r)$ to $F(\mu_s, r)$ is small enough to be masked by the uncertainties in $\rho_0(r)$ and $\rho_b(r)$. A Fermi-distribution-like parametrization of $F(\mu_s, r)$ analogous to those used previously is used to prescribe the form factor $f_s(r)$ in Eq. (3). The values obtained, $c_s=3.452$ fm and $z_s=0.694$ fm, differ slightly from the values for $f_0(r)$. The strength V_s in Eq. (3) is given by $V_s=A t_s[\rho_s/\rho_0]_{\rm vol}/N_s$ where N_s is the normalization of $f_s(r)$.

The Fermi-distribution-like form factors $f_0(r)$ and $f_s(r)$ prescribed from the folding integrals in the preceding discussion retain the principal features of the shape of the target nucleus as modified by finite nucleon size and finite range corrections. The finite size correction common to both relativistic and standard optical models is dominant. It is model independent for the purposes of this comparison. The finite range corrections are small enough that their overall influence is not critical. In particular, the vector effective interaction could be taken as having zero range to within the uncertainties in the finite size correction and the point nucleon baryonic density of the target. The finite range correction for the scalar effective interaction is important only to the extent that it differs from the vector finite range correction. This small difference is both critical and uncertain; it appears to be better determined from low energy nucleon-nucleus scattering than from the scalar-isoscalar component of the two-nucleon interaction.[1,43,51] Thus, unless the mean field approximation used as a guide to the finite range corrections is patently misleading, the form factors $f_0(r)$ and $f_s(r)$ are fairly well determined by rudimentary considerations. This is in marked constrast to the standard optical model where finite range corrections are of paramount importance. It may be the reason why a fixed geometry prescription in the relativistic optical model is a useful starting point for analyses over an extended range of energy and momentum transfer.

The strength parameters V_0 and $V_\cdot$ are subject to considerably greater uncertainty. With the geometry fixed, these are determined from t_0, t_s, and the bulk correction $[\rho_s/\rho_0]_{\rm vol}$. Table 1 of Ref. 1 shows the values of these quantities as obtained from OBEM parameters determined from nucleon-nucleon data and from the mean field theory of nuclear matter. In addition to these uncertainties, we have found that the ratio R_R defined by Eq. (29) is energy dependent[2,42]; it decreases slightly in magnitude with increasing bombarding energy. Thus, the strength parameters prescribed in the preceding discussion are best regarded as initial values in a data analysis fitting procedure. For reference purposes, the values $V_0=383$ MeV and $V_s=-470$ MeV are ob-

tained from $t_0 = 2321$ MeV fm^3, $t_s = -3039$ MeV fm^3, and $[\rho_s/\rho_0]_{nm} = 0.932$ and yield $R_R = -0.819$.

B. Analysis

The potentials $V_0(r)$ and $V_s(r)$ just described provide the starting point for this analysis of the IUCF 181 MeV $\vec{p}$-^{40}Ca elastic scattering data. The form factors $f_0(r)$ and $f_s(r)$ for the real parts of $U_0(r)$ and $U_s(r)$ are kept fixed throughout. The strengths V_0 and V_s are treated as free parameters. This fixed geometry approach to the real parts of $U_0(r)$ and $U_s(r)$ has been used previously to obtain good fits to $\vec{p}$-^{40}Ca elastic scattering data both below[43] and above[42] the transition region of interest here.

The imaginary parts of $U_0(r)$ and $U_s(r)$ are treated phenomenologically with the experimental reaction cross section[52] used as a check on the potentials deduced from the elastic scattering analysis. Initially, the form factors were kept fixed with $g_0(r) = f_0(r)$ and $g_s(r) = f_s(r)$, while the strength parameters W_0 and W_s were treated as free parameters. This approach, which leaves only the four strength parameters available in the fitting procedure, is adequate without modification for analyses above the transition region where volume absorption is prevalent. It is inadequate as a starting point at low energies where surface peaked form factors for $g_0(r)$ and $g_s(r)$ are appropriate. In the present analysis, a fair representation of the elastic scattering data was obtained by varying the strength parameters alone. However, the calculated reaction cross section was inordinately larger than the experimental value. The much better fit to the elastic scattering data shown in Fig. 1 and a significantly lower calculated reaction cross section were obtained by allowing the four strength parameters and the two shape parameters of $g_0(r)$ to vary with those of $g_s(r)$ kept fixed. Other possibilities, such as keeping $g_0(r)$ fixed and allowing the shape parameters of $g_s(r)$ to vary, gave similar results. While a fit comparable to that shown in Fig. 1 could not be obtained by variation of the strength parameters alone, the departure from the fixed geometry prescription for $g_0(r)$ and $g_s(r)$ leading to the results shown is not extreme. The elastic scattering data and the reaction cross section in the transition region are sensitive to small differences in the geometry of the imaginary parts of $U_0(r)$ and $U_s(r)$. The influence of this sensitivity on the shape of the real part of the effective Schrödinger equation central potential described later is slight.

The potential parameters deduced from this analysis are listed in Table I(a) with the fixed geometry parameters underlined. The strengths

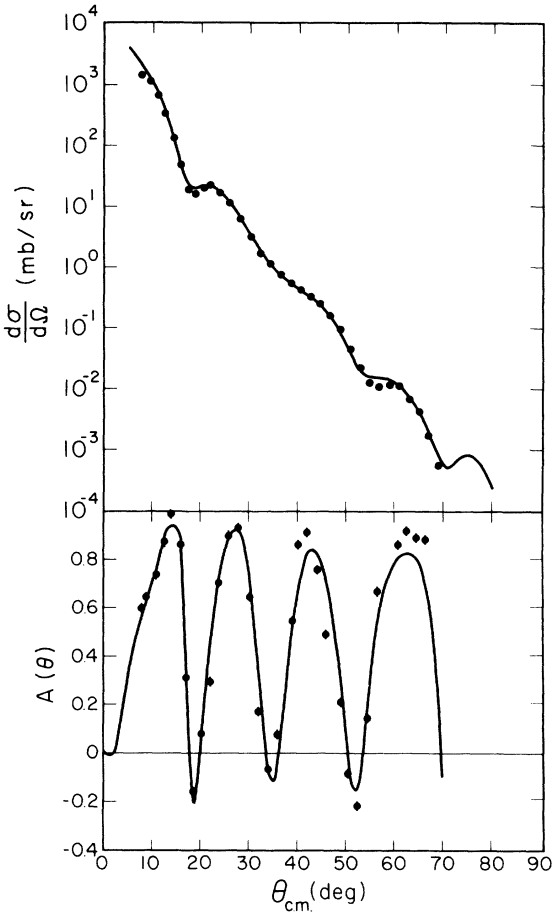

FIG. 1. Elastic $\vec{p}$-^{40}Ca cross sections and analyzing powers at 181 MeV. The smooth curves are the results of the relativistic optical model analysis described in the text.

V_0 and V_s in Table I(a) are each smaller than the mean field theory values given above, and the ratio $R_R = -0.760$ is lower by 7% than the corresponding mean field theory value.

C. Effective Schrödinger equation optical potential

In order to compare results from a Dirac equation based optical model analysis with those from a Schrödinger equation based analysis we begin with a standard reduction of the Dirac equation to second order form. The equation for the upper two components is

$$[p^2 + 2E(U_{\text{eff}} + U_{so}\vec{\sigma}\cdot\vec{L})]\psi_u(\vec{r}) = [(E - V_C)^2 - m^2]\psi_u(\vec{r}), \tag{39}$$

where

TABLE I. (a) The strength and shape parameters for the Lorentz scalar and Lorentz vector potentials determined in the analysis of 181 MeV $\vec{p}$-^{40}Ca data. The numbers in parentheses correspond to the strengths determined from the mean field theory of nuclear matter. The underlined parameters are kept fixed in the analysis. (b) The strength and shape parameters determined from the analysis of 181 MeV $\vec{p}$-^{40}Ca data using the nonrelativistic optical model described in Ref. 55.

Potential	(a) Relativistic potentials Strength (MeV)	c (fm)	z (fm)
$\mathrm{Re}U_0$	334 (383)	3.474	0.668
$\mathrm{Im}U_0$	−107	3.487	0.716
$\mathrm{Re}U_s$	−437 (−470)	3.453	0.692
$\mathrm{Im}U_s$	109	3.453	0.692
Potential	**(b) Nonrelativistic potentials Strength (MeV)**	**c (fm)**	**z (fm)**
$\mathrm{Re}U_{\mathrm{cent}}$	−17.3	4.310	0.780
$\mathrm{Im}U_{\mathrm{cent}}$	− 8.7	4.326	0.645
$\mathrm{Re}U_{so}$	− 2.83	3.523	0.610
$\mathrm{Im}U_{so}$	+ 1.85	3.523	0.610

$$U_{\mathrm{eff}}=\frac{1}{2E}(2EU_0+2mU_s - U_0^2+U_s^2-2V_CU_0+iU_D\vec{r}\cdot\vec{p}) , \quad (40)$$

$$U_{so}=-\frac{1}{2E}\frac{\partial B}{\partial r}\Big/Br=-U_D , \quad (41)$$

and

$$B=(E+m+U_s-U_0-V_C)/(E+m) . \quad (42)$$

This allows us to identify U_{eff} and U_{so} as effective Schrödinger equation central and spin orbit potentials. These effective potentials, constructed from U_0 and U_s, are appropriate for comparing ROM and SOM results.

The radial derivative present in the Darwin term in Eq. (40) can be removed by the substitution

$$\psi_u(\vec{r})=B^{1/2}\phi(\vec{r}) . \quad (43)$$

This relationship between ψ_u and ϕ is analogous to the Perey damping factor[53] for the Schrödinger equation wave function resulting from a nonlocal or velocity dependent potential. The wave equation for ϕ has the same form as Eq. (39) for ψ_u but with U_{eff} written,

$$U_{\mathrm{eff}}=\frac{1}{2E}\left[2EU_0+2mU_s-U_0^2+U_s^2-2V_CU_0 - \frac{1}{2}\frac{1}{Br^2}\frac{\partial}{\partial r}\left(r^2\frac{\partial}{\partial r}B\right)+\frac{3}{4}\frac{1}{B^2}\left(\frac{\partial}{\partial r}B\right)^2\right] . \quad (44)$$

The effect of the Darwin term,

$$U_{\mathrm{Darwin}}=-\frac{1}{2}\frac{1}{Br^2}\left(\frac{\partial}{\partial r}r^2\frac{\partial}{\partial r}B\right)+\frac{3}{4}\frac{1}{B^2}\left(\frac{\partial}{\partial r}B\right)^2 , \quad (45)$$

is most pronounced in the nuclear interior. For the optical potential determined in the present analysis the contribution to the rms radius and volume integral of U_{eff} is negligible.[54] For the calculation given in Sec. IV we neglect the small contribution of V_C to B.

IV. RESULTS AND COMPARISON WITH SCHRÖDINGER EQUATION OPTICAL MODELS

The analysis described in Sec. III B determines the strengths and geometries of the complex Lorentz scalar and Lorentz vector potentials. However, as discussed in Sec. III C, in order to compare with Schrödinger equation based optical models it is necessary to construct the effective Schrödinger central and spin orbit potentials given in Eqs. (40) and (41). We have analyzed the $\vec{p}$-^{40}Ca data using a relativistic form of the Schrödinger equation[55] and find that a fit to the data equivalent to that shown in Fig. 1 can be obtained with the parameters given in Table I(b). In these calculations the complex central potential had Fermi-distribution-like form factors and the complex spin orbit potential had derivatives of Fermi-distribution-like form factors. In Figs. 2 and 3 we compare the results from the Dirac equation based analysis (ROM) as represented by the effective Schrödinger equation central and spin or-

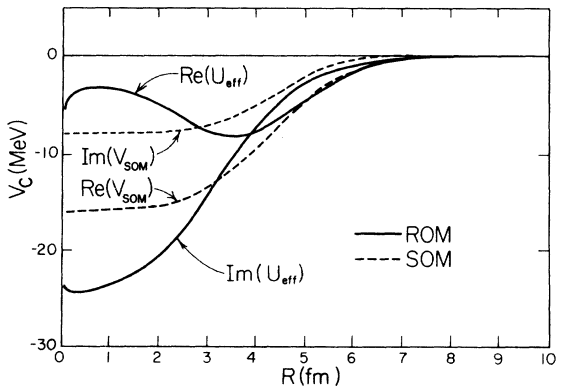

FIG. 2. The smooth curves show the real and imaginary parts of the relativistic effective central potential (ROM) given by Eq. (44) with parameters determined from the analysis $\vec{p}$-^{40}Ca data at 181 MeV. The dashed curves are the corresponding results for the real and imaginary central potentials in the nonrelativistic case (SOM).

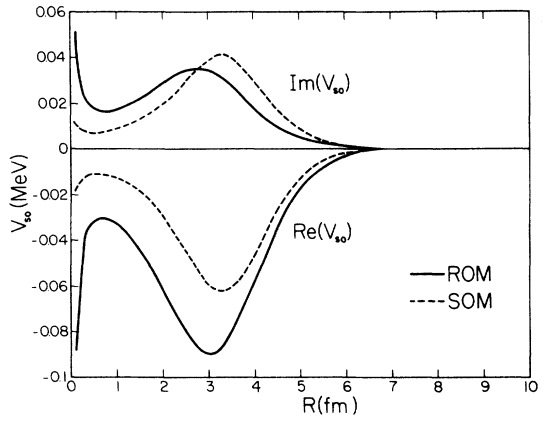

FIG. 3. The smooth curves show the real and imaginary parts of the relativistic effective spin-orbit potential (ROM) given by Eq. (41) with parameters determined from the analysis of $\vec{p}$-^{40}Ca data. The dashed curves are the corresponding results for the real and imaginary spin-orbit potentials in the nonrelativistic case (SOM).

bit potentials with those of the Schrödinger equation based analysis (SOM). The corresponding comparison between ROM and SOM volume integrals and rms radii is given in Table II. These quantities are defined by

$$J=\int U_{\text{eff}}(r)d\vec{\mathrm{r}}/A\,, \tag{46}$$

$$\langle R_c\rangle^{1/2}=\left[\int U_{\text{eff}}(r)r^2 d\vec{\mathrm{r}}\Big/JA\right]^{1/2}, \tag{47}$$

$$K=\int U_{so}(r)d\vec{\mathrm{r}}\Big/A^{1/3}, \tag{48}$$

$$\langle R_{so}\rangle^{1/2}=\left[\int U_{so}(r)r^2 d\vec{\mathrm{r}}\Big/KA^{1/3}\right]^{1/2}. \tag{49}$$

Such integrated quantities have traditionally been used when comparing theory and phenomenology as they are well determined in Schrödinger equation based analyses.

There are a number of differences in the results from these two analyses, perhaps the most interesting being the striking disparity between the real central potentials. The real central ROM potential clearly shows a wine-bottle-bottom shape with drastically reduced attraction in the interior region of the nucleus. Using a Dirac-Hartree approach the Liege[27-30] group found the origin of the unorthodox shape of ReU_{eff} in the transition energy region to be due to the presence of square terms in U_{eff}. They do not consider absorption although it is appreciable in this energy region, and both real and imaginary parts of $U_0(r)$ and $U_s(r)$ contribute to the real and imaginary parts of U_{eff}. Thus, the presence of absorption does alter the real effective potential. However, our calculations show the wine-bottle-bottom shape to occur at 180 MeV even when absorption is present. It is impossible to obtain such behavior from the standard Fermi shape generally employed in nonrelativistic optical model analyses. This fact was recognized by Elton[39] in his 1966 analysis of 180 MeV p-^{56}Fe data and has recently been emphasized by Meyer *et al.*[40] for $\vec{p}$-^{12}C. In both cases a more complicated radial dependence of the real optical potential is required to fit the data. In the case of Meyer *et al.*[40] the optical potential is taken to have a double Woods-Saxon (sum of two Fermi-type functions) form for both central and spin orbit terms. With the twenty-four parameters available a good fit to the data can be achieved. In the relativistic model used here six parameters out of a possible twelve are varied. While the scalar and vector optical potentials themselves have the Fermi-like shape characteristic of nuclear densities, the change in the shape of the real effective Schrödinger equation potential with energy results primarily from the explicit energy dependence of U_{eff} and is a consequence of treating the problem within a relativistic framework.

Considering the pronounced differences between the ROM and SOM real central potentials shown in Fig. 2 it is not surprising that the integrated quantities given in Table II differ substantially. The difference in the rms radii could be expected as the rms radius of the real effective Schrödinger equation potential given by Eq. (47) exhibits a discontinuity as its volume integral goes through zero. This point, discussed some time ago by Humphries[56] is a natural consequence of the model.[30]

Although the imaginary central potentials for both ROM and SOM cases shown in Fig. 2 exhibit Fermi-like shapes of about the same rms radii, they differ considerably in strength. This difference is reflected in the volume integrals given in Table II, one consequence of which is the large difference between the calculated reaction cross sections in the two cases. Neither analysis agrees particularly well with the experimental result of 524 ± 14 mb determined by Johansson *et al.*[49]: the ROM value is about 11% higher than experiment while the SOM result is about 20% lower. There has been a history of optical model calculations which either overestimate or underestimate the p-^{40}Ca reaction cross section at 180 MeV. We suggest that the reaction cross section provides an important experimental constraint in the transition region from 150 to 500 MeV.

It follows from Eq. (41), which gives the effec-

TABLE II. Volume integrals in MeV fm^3 and rms radii in fm for $\vec{p}$-^{40}Ca at 181 MeV calculated from the results of ROM and SOM analysis and theoretical BHF and IA results.

	ROM	SOM	BHF	IA
ReJ (MeV fm^3)	−131	−193	−127	−177
ImJ	−147	− 90	−148	−207
ReK	− 98	− 73	−110	−107
ImK	33	48	22	22
ReR_c (fm)	4.745	4.421	4.90	3.991
ImR_c	3.957	4.120	4.03	3.741
ReR_{so}	3.998	4.010	3.91	4.044
ImR_{so}	3.814	4.010	3.97	4.166
σ_r (mb)	582	412		631

tive Schrödinger equation spin orbit potential, that the real and imaginary rms radii will not be equal and further will differ from the rms radii of the effective central potential. This feature of the mixed potential model is apparent from the values given in Table II. As is shown in Fig. 3 the spin orbit potentials from the ROM and SOM analyses exhibit quantitatively similar behavior. It is worth noting that the energy region near 200 MeV is characterized by very large polarization effects for targets throughout the Periodic Table.[55] These effects yield a strong constraint on the form of the spin orbit potential extracted from optical model analyses. This it is not surprising that the spin orbit potentials obtained from the ROM and SOM analyses are similar, and the values of the volume integrals and rms radii given in Table II reflect this fact.

We attribute the differences between the ROM and SOM results shown in Figs. 2 and 3 and summarized in Table II to the coupling between the effective central and spin orbit potentials in the relativistic model. This coupling effectively constrains the effective central and spin orbit potentials according to the individual strengths and geometries of the Lorentz scalar and vector potentials. The presence of square terms in U_{eff} means that the simple uncoupled relationship between the strength and geometry of the potentials $U_0(r)$ and $U_s(r)$, as was written in Eqs. (2) and (3), does not exist for U_{eff}. In fact, there is considerable correlation between strength and geometry in U_{eff} and to a smaller extent in U_{so}.

It is interesting to note that behavior similar to that shown in Fig. 2 for the real effective central potential occurs in nonrelativistic calculations of the real optical potential such as those of Brieva and Rook[38] using BHF. In Table II a comparison of the integrated quantities characterizing the general features of the optical potential from the ROM and SOM analyses is made with the BHF calculation of Brieva and Rook,[38,57] and with an IA calculation in the KMT approach[58] by one of the present authors (PS), using the two-nucleon t matrix of Love *et al.*[59] Since there are substantial differences between the theoretical calculations as well as between theory and phenomenology, considerable work remains to be done. The analyses of experimental data using the relativistic approach needs to be extended to a number of different energies so that trends can be determined and more meaningful comparison with both Schrödinger equation based analyses and theory can be made.

V. SUMMARY

In this paper we have discussed some of the consequences of using a Dirac equation optical model as an alternative to the standard Schrödinger equation optical model. This approach produces a number of macroscopic features of the optical potential which are quite different from the usual results. We have identified the origin of the unorthodox potential shape with the presence of square terms in the effective Schrödinger equation potential obtained from the reduction of the Dirac equation to second order form. These terms, along with the explicit energy dependence of U_{eff}, give rise to the characteristic features of the real effective optical potential including its change from attraction to repulsion in the transition energy region. There are a number of ways that these features, which do in fact seem to be required by experiment, can be mocked up in a conventional Schrödinger-equation analysis. For example, one could take (as has been done in Ref. 40) each complex central and complex spin-orbit potential to be the sum of two Fermi distributions, each with its own set of parameters. The resulting optical potential, however, is quite complicated in form. It seems to us more desirable and direct to preserve the simplicity of the potentials themselves and use instead a relativistic wave equation containing both Lorentz vector and scalar potentials. Not only does this approach exhibit the fundamental connection between central and spin-orbit effective potentials and their intrinsic energy dependence, but this type of analysis also provides the necessary phenomenological basis for the description of the nuclear many-body problem in terms of meson exchange descriptions of the two-body force.

This work was supported in part by the National Science Foundation under Grant No. PHY-7825532.

[1]L. G. Arnold and B. C. Clark, Phys. Lett. 84B, 46 (1979).
[2]L. G. Arnold, B. C. Clark, and R. L. Mercer, Phys. Rev. C 19, 917 (1979) and references therein.
[3]H. P. Duerr, Phys. Rev. 103, 469 (1956).
[4]L. D. Miller, Phys. Rev. Lett. 28, 1281 (1972).
[5]L. D. Miller and A. E. S. Green, Phys. Rev. C 5, 241 (1972).
[6]L. D. Miller, Phys. Rev. C 9, 537 (1974); 14, 706 (1976).
[7]L. D. Miller, Ann. Phys. (N. Y.) 91, 40 (1975).
[8]J. V. Noble, Phys. Rev. C 17, 2151 (1978); 20, 255 (1979); Phys. Rev. Lett. 43, 100 (1979).
[9]J. V. Noble, Nucl. Phys. A329, 354 (1979).
[10]G. A. Miller and J. V. Noble, Phys. Rev. C 21, 2519 (1980).
[11]M. Bosterli, in *Advances in Nuclear Science*, edited by J. W. Negele and E. Vogt (Plenum, New York, 1979), Vol. 11, p. 367 and references therein; Phys. Rev. D 22, 437 (1980).
[12]R. Brockmann and W. Weise, Phys. Rev. C 16, 1282 (1977).
[13]R. Brockmann, Phys. Rev. C 18, 1510 (1978).
[14]J. Boguta and J. Rafelski, Phys. Lett. 71B, 22 (1977).
[15]J. Boguta and A. R. Bodmer, Nucl. Phys. A292, 413 (1977).
[16]J. Boguta, LBL Reports Nos. 11465–11468, 1980.
[17]K. P. Lohs and J. Hüfner, Nucl. Phys. A296, 349 (1978).
[18]J. D. Walecka, Ann. Phys. (N. Y.) 83, 491 (1974).
[19]J. D. Walecka, Phys. Lett. 94B, 293 (1980).
[20]F. E. Serr and J. D. Walecka, Phys. Lett. 79B, 10 (1978).
[21]B. D. Serot, Phys. Lett. 86B, 146 (1979).
[22]B. D. Serot and J. D. Walecka, Phys. Lett. 87B, 172 (1979).
[23]S. A. Chin, Ann. Phys. (N. Y.) 108, 301 (1977).
[24]M. Brittan, Phys. Lett. 79B, 27 (1978).
[25]L. C. Liu and C. M. Shakin, Phys. Rev. C 20, 1195 (1979).
[26]M. R. Anastasio, L. S. Celenza, and C. M. Shakin, Phys. Rev. Lett. 45, 2096 (1980).
[27]M. Jaminon, C. Mahaux, and P. Rochus, Phys. Rev. Lett. 43, 1097 (1979).
[28]C. Mahaux, in *Common Problems in Low- and Medium-Energy Nuclear Physics*, edited by B. Castel, B. Coulard, and F. C. Khanna (Plenum, New York, 1979), p. 265.
[29]M. Jaminon and C. Mahaux, in *Proceedings of the Conference on the Meson Theory of Nuclear Forces and Nuclear Matter, Bad Honnef, 1979*, edited by D. Schütte, K. Holinde, and K. Bleuler (Bibliographisches Institut AG, Zürich, 1980).
[30]M. Jaminon, C. Mahaux, and P. Rochus, Phys. Rev. C 22, 2027 (1980).
[31]J. M. Eisenberg, TAUP Report No. 871, 1980.
[32]We refer to a relativistic optical model (ROM) as an optical model which uses the Dirac, Klein-Gordon, or other covariant wave equation as the relevant wave equation in contrast to the standard optical model (SOM) which is based on the use of the Schrödinger equation with or without relativistic kinematic corrections.
[33]R. J. Glauber, in *Lectures in Theoretical Physics*, edited by W. E. Brittin *et al.* (Interscience, New York, 1959), Vol. I, p. 315.
[34]A. K. Kerman, H. McManus, and R. M. Thaler, Ann. Phys. (N. Y.) 8, 557 (1959).
[35]K. M. Watson, Phys. Rev. 89, 575 (1958).
[36]J.-P. Jeukenne, A. Lejeune, and C. Mahaux, Phys. Rev. C 16, 80 (1977); Phys. Rep. 25C, 83 (1976).
[37]C. Mahaux, in *Microscopic Optical Potentials*, edited by H. V. von Geramb (Springer, New York, 1979), p. 1.
[38]F. A. Brieva and J. R. Rook, Nucl. Phys. A291, 299 (1977); A291, 317 (1977); A297, 206 (1978); A307, 493 (1978).
[39]L. R. B. Elton, Nucl. Phys. 89, 69 (1966).
[40]H. O. Meyer, P. Schwandt, G. L. Moake, and P. P. Singh, Phys. Rev. C 23, 616 (1981).
[41]L. G. Arnold, B. C. Clark, and R. L. Mercer, Lett. Nuovo Cimento 18, 151 (1977); Report No. OSU-TR 201, 1976).
[42]B. C. Clark, L. G. Arnold, and R. L. Mercer, Bull. Am. Phys. Soc. 25, 520 (1980); 25, 741 (1980).
[43]L. G. Arnold, B. C. Clark, and R. L. Mercer, in *Proceedings of the Workshop on Nuclear Structure with Intermediate Energy Probes*, Los Alamos Scientific Laboratory, 1980; Phys. Rev. C 23, 15 (1981).
[44]The possibility of using different structure profiles in relating $\tilde{\rho}_0(r)$ and $\tilde{\rho}_s(r)$ to their respective point densitites is discussed following Eq. (35).
[45]J. W. Negele, Phys. Rev. C 1, 1260 (1970).
[46]W. D. Myers, Nucl. Phys. A204, 465 (1973).
[47]J. S. McCarthy, I. Sick, and R. R. Whitney, Phys. Rev. C 15, 1396 (1977).
[48]G. W. Greenless, G. J. Pyle, and Y. C. Tang, Phys. Rev. 171, 1115 (1968).
[49]In relativistic models, there are four nuclear ground state densities if neutrons and protons are treated separately.
[50]Equation (35) with $[\rho_s/\rho_0]_{\rm vol}$ approximated by $[\rho_s/\rho_0]_{nm}$ was used in Ref. 1 and resulted in an effective Schrödinger equation central potential for ^{40}Ca that was slightly weaker than the real part of the empirical optical potential at low energies. A slightly larger value of $[\rho_s/\rho_0]_{\rm vol}$ than used in Ref. 1 is suggested by Eq. (19) and would resolve this discrepancy.
[51]Figure 1 of Ref. 1 shows the effect of varying μ_s on the rms radii of the effective Schrödinger equation potentials for ^{40}Ca.
[52]A. Johansson, U. Svanberg, and P. E. Hodgson, Ark. Fys. 19, 541 (1961).
[53]F. G. Perey, in *Direct Interaction and Nuclear Reaction Mechanisms*, edited by E. Clementel and C. Villi (Gordon and Breach, New York, 1963), p. 125.
[54]In the present analysis the real and imaginary volume integrals are changed by less than 1% and the real and imaginary rms radii by less than 2%.
[55]A. Nadasen, P. Schwandt, P. P. Singh, W. W. Jacobs, A. D. Bacher, P. T. Debevec, M. D. Kaitchuck, and J. T. Meek; Phys. Rev. C 23, 1023 (1981).
[56]R. Humphreys, Nucl. Phys. A183, 580 (1972).
[57]F. A. Brieva, private communication.
[58]P. Schwandt, F. Petrovich, and A. Picklesimer, IUCF Annual Technical and Scientific Report 1978, p. 27.
[59]W. G. Love, A. Scott, F. T. Baker, W. P. Jones, and J. D. Wiggins, Phys. Lett. 73B, 277 (1978); and W. G. Love, private communication.